



OPEN

Amide proton transfer weighted (APT_w) imaging based radiomics allows for the differentiation of gliomas from metastases

Elisabeth Sartoretti^{1,2,8}, Thomas Sartoretti^{1,2,8}, Michael Wyss^{1,3}, Carolin Reischauer^{4,5}, Luuk van Smoorenburg¹, Christoph A. Binkert¹, Sabine Sartoretti-Schefer¹ & Manoj Mannil^{6,7}✉

We sought to evaluate the utility of radiomics for Amide Proton Transfer weighted (APT_w) imaging by assessing its value in differentiating brain metastases from high- and low grade glial brain tumors. We retrospectively identified 48 treatment-naïve patients (10 WHO grade 2, 1 WHO grade 3, 10 WHO grade 4 primary glial brain tumors and 27 metastases) with either primary glial brain tumors or metastases who had undergone APT_w MR imaging. After image analysis with radiomics feature extraction and post-processing, machine learning algorithms (multilayer perceptron machine learning algorithm; random forest classifier) with stratified tenfold cross validation were trained on features and were used to differentiate the brain neoplasms. The multilayer perceptron achieved an AUC of 0.836 (receiver operating characteristic curve) in differentiating primary glial brain tumors from metastases. The random forest classifier achieved an AUC of 0.868 in differentiating WHO grade 4 from WHO grade 2/3 primary glial brain tumors. For the differentiation of WHO grade 4 tumors from grade 2/3 tumors and metastases an average AUC of 0.797 was achieved. Our results indicate that the use of radiomics for APT_w imaging is feasible and the differentiation of primary glial brain tumors from metastases is achievable with a high degree of accuracy.

Abbreviations

APT _w	Amide Proton Transfer weighted
ML	Machine learning
TA	Texture analysis
GLRLM	Gray-level run length matrix
GLSZM	Gray-level size zone matrix
NGTDM	Neighbouring gray tone difference matrix
GLDM	Gray-level dependence matrix
CEST	Chemical Exchange Saturation Transfer

Amide proton transfer weighted (APT_w) imaging represents a novel contrast media free molecular MR imaging technique that has recently shown promise in characterizing and differentiating brain neoplasms as well as malignancies in other body regions¹⁻⁷. The APT_w signal originates from amide protons in endogeneous proteins and peptides in the parenchyma. In tumor tissue, the content of mobile proteins and peptides is increased thus resulting in increased APT_w signal intensity values^{8,9}.

¹Institute of Radiology, Kantonsspital Winterthur, Winterthur, Switzerland. ²Faculty of Medicine, University of Zürich, Zürich, Switzerland. ³Philips Healthsystems, Zürich, Switzerland. ⁴Department of Medicine, University of Fribourg, Fribourg, Switzerland. ⁵Department of Radiology, HFR Fribourg-Hôpital Cantonal, Fribourg, Switzerland. ⁶Department of Neuroradiology, Kantonsspital Aarau, Aarau, Switzerland. ⁷Institute of Clinical Radiology, University Hospital Münster, University of Münster, Albrecht-Schweitzer-Campus 1, E48149 Münster, Germany. ⁸These authors contributed equally: Elisabeth Sartoretti and Thomas Sartoretti. ✉email: manoj.mannil@ukmuenster.de

	3D APTw sequence
FOV	228 × 178 × 60 mm ³
Scan mode; Acquisition voxel; Reconstruction voxel	3D; 1.8 × 1.8 × 6.0 mm ³ ; 0.9 × 0.9 × 3.85 mm ³
Reconstruction matrix	256 × 256
Slice thickness, Slice gap	3.85 mm, 0 mm
SENSE or Compressed SENSE factor	1.6 SENSE
TSE factor	174
Rest slabs	0
Flip angle (in degrees)	90
TR, TE and TE equivalent	TR 5800 to 5864 ms; TE 7.8 to 8.3 ms
Inversion time TI	–
Fat suppression	SPiR
APTw	saturation B _{1, rms} : 2 μT; saturation duration: 2 s
Number of acquisitions NSA	1
Scan duration	03 min 42 s

Table 1. APTw MRI sequence parameters.

With the exception of one study¹⁰, these previous investigations utilized standard histogram analyses techniques at the most to analyse the APTw signal of the tissue at hand thus only scratching the surface of the information that can potentially be extracted from radiological images^{1–3}.

With recent advances in the field of machine learning (ML), radiomics techniques allowing for the extraction of high-dimensional mineable data from medical images have been developed and introduced to medical imaging thus enabling in-depth tissue classification and characterization^{11–15}.

In this proof-of-concept study we aimed at assessing the potential of radiomics and ML for APTw imaging. To this extent, we used radiomics on APTw images to differentiate WHO Grade 2, 3 and 4 gliomas from brain metastases.

Materials and methods

This study received institutional review board approval (Cantonal Ethical Committee Zürich, Switzerland) and was performed in accordance with all guidelines and regulations defined by the institutional review board. All subjects gave written informed general consent.

Subjects. In this retrospective study we included 48 patients (mean age: 61 years, range: 37–83 years) diagnosed with either low- or high grade gliomas (10 patients with WHO Grade 2 tumors, 1 patient with WHO Grade 3 tumor and 10 patients with WHO Grade 4 tumors (= glioblastoma) or brain metastases (MET; 27 patients, with 15 lung, 1 breast, 9 melanoma and 2 kidney as primary sites of origin). Initially 64 consecutive patient studies acquired between august 2018 and april 2020 at a single tertiary institution were reviewed. Then the following exclusion criteria were applied: < 18 years, lack of histological analysis of neoplasm (6 patients), unavailable MRI data (1 patient), treatment prior to MRI, lesions with a diameter of under 10 mm¹⁶ (3 patients), failure to compute APTw signal intensities during image reconstruction (6 patients). In the case of multiple metastases all lesions were used for analysis (if they fulfilled size requirements) and were pooled¹⁷ thus resulting in one data point per patient. A flowchart can be found in the *supplementary material*.

MR imaging. Subjects were examined on a clinical 3 T scanner (Achieva, Philips Healthcare, Best, the Netherlands) with an eight channel receive-only head coil array. The following sequences were acquired: precontrast transverse diffusion-weighted imaging (DWI), 3D double inversion recovery (DIR), 3D T1-weighted (T1w) turbo field echo (TFE) and postcontrast 3D fluid attenuated inversion recovery (FLAIR), 3D T1 black blood turbo spin echo (TSE) or 3D T1w m-Dixon TFE, APTw and 2D T2w TSE.

Table 1 shows the sequence parameters for the APTw sequence.

We used a clinically approved APTw sequence^{18–20} acquired in transverse oblique orientation parallel to the intercommissural line. 16 slices with a slice thickness of 3.85 mm were acquired. The first slice was centered at the inferior border connecting the rostrum and the splenium of the corpus callosum^{19,20}. Details on how APTw imaging contrast was generated can be found in the *supplementary material*.

Radiomics feature extraction and image analysis. APTw and postcontrast T1w or FLAIR Digital Imaging and Communications in Medicine (DICOM) files were loaded into the open-source software platform 3D Slicer (v. 4.10.2) and were aligned geometrically. Subsequently, two readers (TS and ES each with 3 years of experience) manually segmented the neoplasms on overlaid images according to contrast enhancement and solid parts of neoplasms²¹. Segmentation was performed on all axial slices for 3D segmentation of either T1w postcontrast or FLAIR images superficially overlaid onto the APTw images (Fig. 1). Specifically, readers outlined neoplasms on pseudo-images that were generated by accurately overlaying APTw with the now geometrical identical structural images. These pseudo-images contain the APTw imaging information but visually reflect

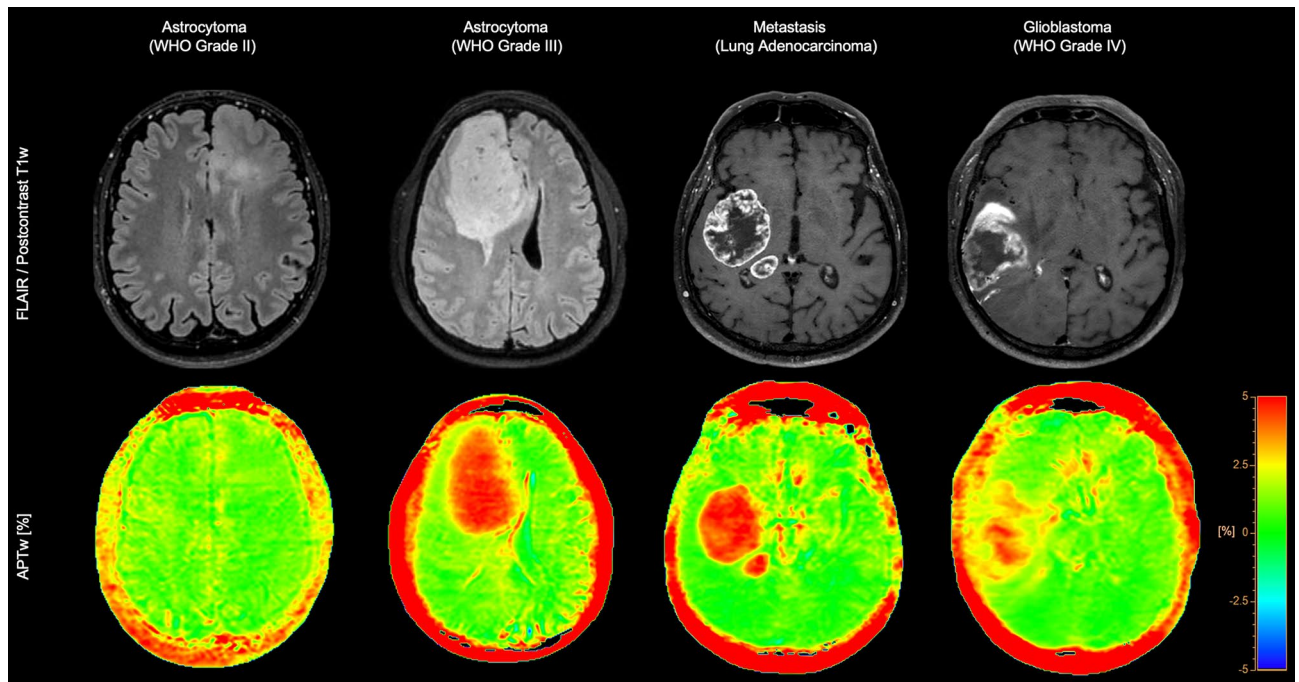


Figure 1. Representative image examples of 4 patients who presented with different neoplasms. FLAIR or T1w postcontrast images are provided in the top row, while the corresponding APTw images are shown in the bottom row.

T1w postcontrast or FLAIR images. Intensity discretization was performed to a bin width of 25. Gray level cooccurrence matrix (GLCM) features were computed at 4 inter-pixel distances.

Then 110 radiomics features were extracted with the built-in pyRadiomics package implemented into 3D Slicer²². Most features are in accordance with those described in the Imaging Biomarker Standardization Initiative (IBSI)²³. Radiomics features corresponded to seven different matrices/feature classes: First-order statistics/histogram matrix, shape-based features, gray-level cooccurrence matrix (GLCM), gray-level run length matrix (GLRLM), gray-level size zone matrix (GLSZM), neighbouring gray tone difference matrix (NGTDM), and gray-level dependence matrix (GLDM). A detailed overview and description of radiomics features can be found elsewhere^{22,24}.

Radiomics features—dimension reduction. Dimension reduction was performed in two steps. First, radiomics features of both readers were compared by means of intraclass correlation coefficients (ICC). ICC values of greater than 0.8 were interpreted as excellent agreement^{11,25}. Radiomics features with ICC values below this threshold were discarded from further analysis, as shown previously²⁶. In a second step, a classifier attribute evaluation filter (CfsSubsetEval) of the open source software package Weka (WEKA, version 3.8.3, University of Waikato, Hamilton, New Zealand) were applied on the training data to evaluate the worth of an attribute. This method measures the significance of attributes on the basis of predictive ability of attributes and its degree of redundancy. The subsets which are having less intercorrelation but are highly correlated to the target class are selected for further analyses.

The remaining radiomics features were then used to train ML classifiers. Combinations of the weighted radiomics features were used then to distinguish metastases from glial primary brain tumours.

For the consecutive subanalyses of distinguishing glioblastomas from other glial brain tumors and metastases, we performed a prior principal component analysis to cover approximately 95% of variance in the original dataset.

Machine learning. For ML analysis, open-source software (WEKA, version 3.8.3, University of Waikato, Hamilton, New Zealand) was used. For prediction of histopathology, a commonly-used ML algorithm implemented in the open source WEKA package was tested with handpicked hyperparameters: Multilayer perceptron, which uses backpropagation to learn a multi-layer perceptron to classify instances with a learning rate of 0.3 and a momentum of 0.2. For further subanalyses we used a random forest classifier. All results were tenfold cross validated to overcome overfitting.

Results

Dimension reduction. After dimension reduction regarding reproducibility and attribute evaluation, eight out of 110 radiomics features remained for further analysis (Table 2).

#	Radiomics features
1	Voxel volume
2	Mesh volume
3	Dependence Non uniformity normalized
4	Large dependence high gray level emphasis
5	Low gray level emphasis
6	Sum average
7	Zone variance
8	Zone percentage

Table 2. Radiomics features after dimension reduction.

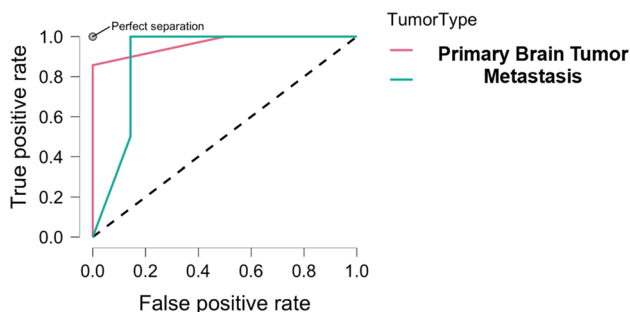


Figure 2. Receiver-operating-characteristics (ROC) of the machine learning algorithm to correctly identify primary brain tumors and metastases. The overall area-under-the-curve (AUC) was 0.836.

Machine learning. The Multilayer Perceptron classifier yielded a sensitivity of 81.3%, a specificity of 81.1%, a recall of 0.81, F-measure 0.81, and an area under the curve (AUC) in receiver operating characteristics (ROC) of 0.836 (Fig. 2) in distinguishing primary brain tumors (glial tumors and glioblastomas) from metastases.

Subanalysis I. In the subanalysis of primary brain tumors, the random forest classifier was able to distinguish glioblastomas from other glial cell tumors (WHO I-III) with a sensitivity of 90.5%, a specificity of 90.4%, a recall of 0.905, F-measure 0.905, and an area under the curve in receiver operating characteristics of 0.868.

Subanalysis II. In the subanalysis of primary brain tumors combined with metastases (Figs. 3, 4), the random forest classifier was able to distinguish these entities with an average sensitivity of 62.5%, a specificity of 74.9%, a recall of 0.625, F-measure 0.628, and an area under the curve in receiver operating characteristics of 0.797 after stratified tenfold cross validation.

Discussion

In this proof-of-concept study we assessed the utility of radiomics for APTw imaging. To this end, we used radiomics features and machine learning algorithms to differentiate glioblastomas from gliomas and brain metastases. Our results indicate that the application of radiomics to APTw imaging is feasible and allows for the differentiation of these brain neoplasms.

APT_w is a novel molecular MRI technique that relies on endogenous cellular proteins in vivo to generate contrast. APT_w imaging belongs to the chemical exchange saturation transfer (CEST) imaging group and is the only form of CEST imaging that has yet achieved FDA approval.

The APT_w signal is theoretically caused by two major sources: Firstly, the intracellular water-exchangeable amide proton content in the cytoplasm and secondly the base-catalyzed exchange rate at physiological pH range²⁷. Incidentally however, the APT_w signal is not pure and may be contaminated by a variety of sources^{28–33}. Specifically, the water longitudinal relaxation time (T₁) may influence the APT_w signal. T₁ effects (T₁ recovery and T₁ related saturation) may influence the APT_w signal linearly or in a more complex manner depending on the level of direct water saturation effects, the field strengths of the MR scanner, irradiation power and whether non-steady-state or steady-state acquisitions are performed. Furthermore, the APT_w signal may also be affected by semi-solid magnetization-transfer (MT) effects and other nearby CEST and relayed nuclear Overhauser enhancement (rNOE) saturation transfer effects. Ultimately, APT_w intensity values may also be impacted by B₁ effects which can be triggered by an imperfect distribution of the irradiation power across the brain.

Currently, APT_w is mainly used for brain tumor imaging. With malignant brain tumors exhibiting a high degree of protein content, the APT_w signal increases steadily with the amount of protein content relative to the surrounding parenchyma. This has been successfully leveraged for differentiating and grading tumors according

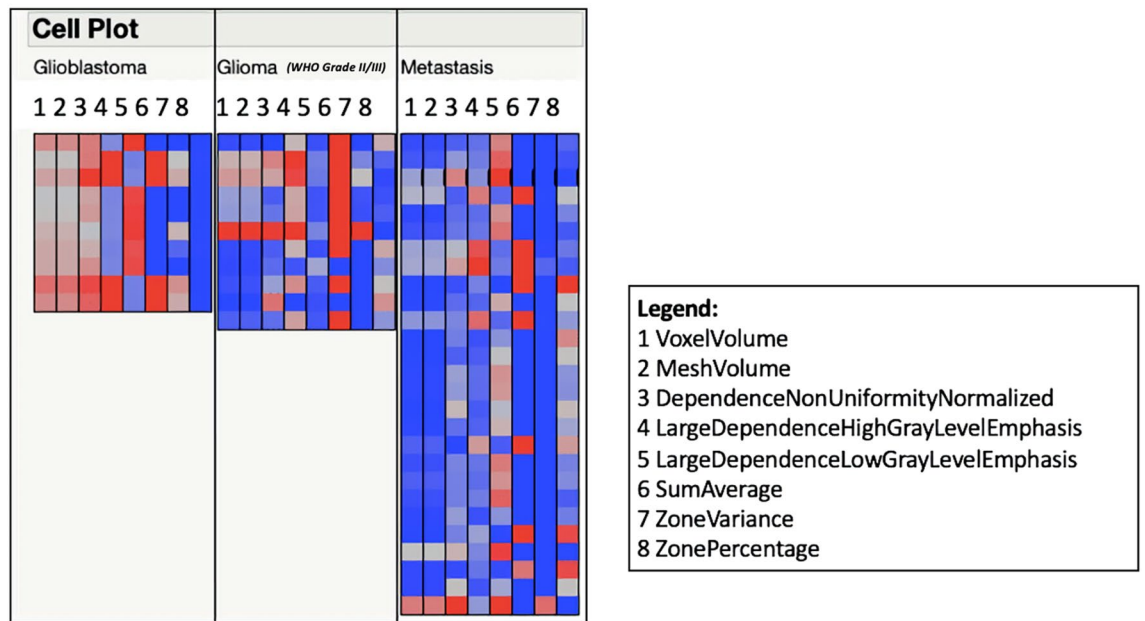


Figure 3. Cell plot of eight standardized Radiomics features visualize similarities between glioblastomas, other gliomas and metastases. Stark differences can be observed in the values of glioblastomas and metastases.

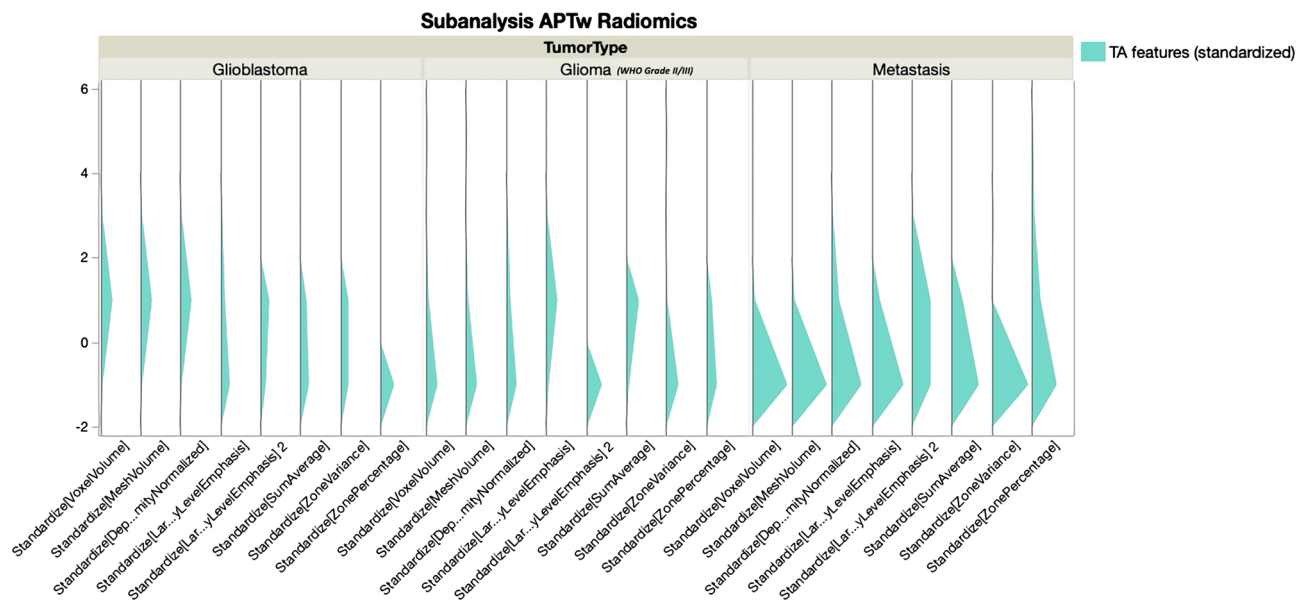


Figure 4. Relative visualization of the eight standardized texture analysis features for glioblastomas, other gliomas and metastases. Overall lower values are observed for metastases compared to glioblastomas and other gliomas, respectively.

to their WHO grade³⁴. Specifically, a recent meta-analysis listed the sensitivity and specificity of APTw for differentiating high grade from low-grade glial tumors as 88% and 91% respectively³⁵. Furthermore, based on this principle, high grade regions can be identified within histologically heterogeneous brain tumors, thus allowing for more accurate sampling during stereotactic biopsies. Additionally, APTw has also been successfully employed for monitoring tumor response to therapies such as radio-/chemotherapy or high-intensity focused ultrasound. Most importantly, APTw enables the differentiation of recurrent tumor from treatment effects such as radiation necrosis. Lastly, APTw has also been successfully used for identifying genetic markers in gliomas, such as the MGMT or IDH status³⁴.

While APTw has already proven to be a valuable addition to the field of tumor imaging, the development of innovative approaches to further leverage the potential of APTw is highly desirable. Radiomics has become a popular method for extracting more data from radiological images thus enabling in-depth study of the tissue at

hand^{12,36}. Therein numerous studies have shown that radiomics approaches based on various imaging modalities (i.e. T1w, T2w, FLAIR, DWI, ADC, SWI, DTI) enhance brain tumor imaging^{12,16,21}.

Here we further enhance the spectrum of radiomics in terms of 3D texture analysis (TA) for brain tumor imaging by applying it to APTw imaging. Our approach yielded a high degree of accuracy in differentiating different types of brain tumors. After dimension reduction all first order TA features were excluded from further analyses due to high intercorrelation. A total of eight features remained for further analysis:

(1) *Dependence Non-Uniformity Normalized (DNN)*, which measures the similarity of voxel dependence throughout the image, an indirect measure of homogeneity. (2) *LargeDependenceHighGrayLevelEmphasis (LDH-GLE)*, which measures the joint distribution of large dependence of higher gray-level values. (3) *Low Gray Level Emphasis (LGLE)*, which measures the distribution of low gray-level values, and (4) *SumAverage*, which measures the relationship between occurrences of pairs with lower intensity values and occurrences of pairs with higher intensity values. All four aforementioned features are derived from the *GrayLevelDependenceMatrix (GLDM)*, which are used to quantify gray level dependencies in a medical image by taking into account neighbouring voxels. The remaining features were associated with the size of the neoplasms. While *VoxelVolume* and *Mesh-Volume* are directly correlated with size, *ZoneVariance* measures the variance in zone size volumes. Similarly, *ZonePercentage* takes into account the number of zones and number of voxels within a defined region of interest, which represents the coarseness of texture. While gliomas were found to exhibit a larger overall size than metastases, which was reflected in these features, they may have no true biological value as metastases and gliomas can present with various sizes.

A major limitation of the current study is its retrospective, single centre design and its small sample size with heterogeneous spectrum of pathologies. It should however be noted, that due to the novelty of the imaging modality (i.e. clinical approval of the sequence occurred in 2018) a larger dataset is not available at the time. Furthermore, larger datasets are likely to decrease the risk of overfitting the machine learning classifiers. We counteracted these limitations by implementing tenfold cross validation of our results. Moreover, the quality of segmentations may strongly influence radiomics results³⁷. Two readers segmented the neoplasms and subsequently features with low interreader agreement were excluded thus reducing bias. However, we acknowledge that there may be more sophisticated methods of performing segmentations and of reducing reader bias. Lastly, our study was performed on a single MR scanner, which limits the generalizability of our findings. The influence of different acquisition parameters, sequences, field strengths, and MR scanners on 3D TA features in APTw images remains to be investigated.

In conclusion, we show that radiomics allows for the differentiation of various brain neoplasms on APTw images. The current work justifies the further study and development of radiomics for APTw imaging in an effort to widen the applicability and utility of APTw imaging for various diseases and anatomies.

Data availability

Data can be made available upon reasonable request to the corresponding author.

Received: 29 November 2020; Accepted: 24 February 2021

Published online: 09 March 2021

References

- Park, J. E., Kim, H. S., Park, K. J., Choi, C. G. & Kim, S. J. Histogram analysis of amide proton transfer imaging to identify contrast-enhancing low-grade brain tumor that mimics high-grade tumor: Increased accuracy of MR perfusion. *Radiology* **277**(1), 151–161. <https://doi.org/10.1148/radiol.2015142347> (2015).
- Yu, H. *et al.* Applying protein-based amide proton transfer MR imaging to distinguish solitary brain metastases from glioblastoma. *Eur. Radiol.* **27**(11), 4516–4524. <https://doi.org/10.1007/s00330-017-4867-z> (2017).
- Takayama, Y. *et al.* Amide proton transfer MR imaging of endometrioid adenocarcinoma: association with histologic grade. *Radiology* **286**(3), 909–917. <https://doi.org/10.1148/radiol.2017170349> (2018).
- Joo, B. *et al.* Amide proton transfer imaging might predict survival and IDH mutation status in high-grade glioma. *Eur. Radiol.* **29**(12), 6643–6652. <https://doi.org/10.1007/s00330-019-06203-x> (2019).
- Seo, N. *et al.* Liver MRI with amide proton transfer imaging: feasibility and accuracy for the characterization of focal liver lesions. *Eur. Radiol.* <https://doi.org/10.1007/s00330-020-07122-y> (2020).
- Qamar, S. *et al.* Pre-treatment amide proton transfer imaging predicts treatment outcome in nasopharyngeal carcinoma. *Eur. Radiol.* <https://doi.org/10.1007/s00330-020-06985-5> (2020).
- Lee, J. B. *et al.* Repeatability of amide proton transfer-weighted signals in the brain according to clinical condition and anatomical location. *Eur. Radiol.* **30**(1), 346–356. <https://doi.org/10.1007/s00330-019-06285-7> (2020).
- Zhou, J., Payen, J. F., Wilson, D. A., Traystman, R. J. & van Zijl, P. C. Using the amide proton signals of intracellular proteins and peptides to detect pH effects in MRI. *Nat. Med.* **9**(8), 1085–1090. <https://doi.org/10.1038/nm907> (2003).
- Zhou, J. *et al.* Differentiation between glioma and radiation necrosis using molecular magnetic resonance imaging of endogenous proteins and peptides. *Nat. Med.* **17**(1), 130–134. <https://doi.org/10.1038/nm.2268> (2011).
- Han, Y. *et al.* Amide proton transfer imaging in predicting isocitrate dehydrogenase 1 mutation status of grade II/III gliomas based on support vector machine. *Front. Neurosci.* **14**, 144. <https://doi.org/10.3389/fnins.2020.00144> (2020).
- Baessler, B. *et al.* Subacute and chronic left ventricular myocardial scar: accuracy of texture analysis on nonenhanced cine MR images. *Radiology* **286**(1), 103–112. <https://doi.org/10.1148/radiol.2017170213> (2018).
- Gillies, R. J., Kinahan, P. E. & Hricak, H. Radiomics: Images are more than pictures, they are data. *Radiology* **278**(2), 563–77. <https://doi.org/10.1148/radiol.2015151169> (2016).
- Hashido, T., Saito, S. & Ishida, T. A radiomics-based comparative study on arterial spin labeling and dynamic susceptibility contrast perfusion-weighted imaging in gliomas. *Sci. Rep.* **10**(1), 6121. <https://doi.org/10.1038/s41598-020-62658-9> (2020).
- Mannil, M. *et al.* Prognostic value of texture analysis from cardiac magnetic resonance imaging in patients with Takotsubo syndrome: A machine learning based proof-of-principle approach. *Sci. Rep.* **10**(1), 20537. <https://doi.org/10.1038/s41598-020-76432-4> (2020).
- Nakamoto, T. *et al.* Prediction of malignant glioma grades using contrast-enhanced T1-weighted and T2-weighted magnetic resonance images based on a radiomic analysis. *Sci. Rep.* **9**(1), 19411. <https://doi.org/10.1038/s41598-019-55922-0> (2019).

16. Ortiz-Ramón, R., Larroza, A., Ruiz-España, S., Arana, E. & Moratal, D. Classifying brain metastases by their primary site of origin using a radiomics approach based on texture analysis: a feasibility study. *Eur. Radiol.* **28**(11), 4514–4523. <https://doi.org/10.1007/s00330-018-5463-6> (2018).
17. Beckers, R. C. J. *et al.* CT texture analysis in colorectal liver metastases and the surrounding liver parenchyma and its potential as an imaging biomarker of disease aggressiveness, response and survival. *Eur. J. Radiol.* **102**, 15–21. <https://doi.org/10.1016/j.ejrad.2018.02.031> (2018).
18. Togao, O. *et al.* Scan-rescan reproducibility of parallel transmission based amide proton transfer imaging of brain tumors. *J. Magn. Reson. Imaging* **42**(5), 1346–1353. <https://doi.org/10.1002/jmri.24895> (2015).
19. Sartoretti, T. *et al.* Amide proton transfer contrast distribution in different brain regions in young healthy subjects. *Front. Neurosci.* **13**, 520. <https://doi.org/10.3389/fnins.2019.00520> (2019).
20. Sartoretti, E. *et al.* Amide proton transfer weighted imaging shows differences in multiple sclerosis lesions and white matter hyperintensities of presumed vascular origin. *Front. Neurol.* **10**, 1307. <https://doi.org/10.3389/fneur.2019.01307> (2019).
21. Li, Z. *et al.* Differentiating brain metastases from different pathological types of lung cancers using texture analysis of T1 postcontrast MR. *Magn. Reson. Med.* **76**(5), 1410–1419. <https://doi.org/10.1002/mrm.26029> (2016).
22. van Griethuysen, J. J. M. *et al.* Computational radiomics system to decode the radiographic phenotype. *Cancer Res.* **77**(21), e104–e107. <https://doi.org/10.1158/0008-5472.CAN-17-0339> (2017).
23. Zwanenburg, A. *et al.* The image biomarker standardization initiative: Standardized quantitative radiomics for high-throughput image-based phenotyping. *Radiology* **295**(2), 328–338. <https://doi.org/10.1148/radiol.2020191145> (2020).
24. Baessler, B. *et al.* Radiomics allows for detection of benign and malignant histopathology in patients with metastatic testicular germ cell tumors prior to post-chemotherapy retroperitoneal lymph node dissection. *Eur. Radiol.* **30**(4), 2334–2345. <https://doi.org/10.1007/s00330-019-06495-z> (2020).
25. Landis, J. R. & Koch, G. G. The measurement of observer agreement for categorical data. *Biometrics* **33**(1), 159–174 (1977).
26. Mannil, M., Burgstaller, J. M., Held, U., Farshad, M. & Guggenberger, R. Correlation of texture analysis of paraspinous musculature on MRI with different clinical endpoints: Lumbar Stenosis Outcome Study (LSOS). *Eur. Radiol.* **29**(1), 22–30. <https://doi.org/10.1007/s00330-018-5552-6> (2019).
27. Heo, H. Y. *et al.* Improving the detection sensitivity of pH-weighted amide proton transfer MRI in acute stroke patients using extrapolated semisolid magnetization transfer reference signals. *Magn. Reson. Med.* **78**(3), 871–880. <https://doi.org/10.1002/mrm.26799> (2017).
28. By, S. *et al.* Amide proton transfer CEST of the cervical spinal cord in multiple sclerosis patients at 3T. *Magn. Reson. Med.* **79**(2), 806–814. <https://doi.org/10.1002/mrm.26736> (2018).
29. Zhang, Z. *et al.* Reduction of transmitter B1 inhomogeneity with transmit SENSE slice-select pulses. *Magn. Reson. Med.* **57**(5), 842–847. <https://doi.org/10.1002/mrm.21221> (2007).
30. Sun, P. Z., Farrar, C. T. & Sorensen, A. G. Correction for artifacts induced by B(0) and B(1) field inhomogeneities in pH-sensitive chemical exchange saturation transfer (CEST) imaging. *Magn. Reson. Med.* **58**(6), 1207–1215. <https://doi.org/10.1002/mrm.21398> (2007).
31. Zu, Z. Towards the complex dependence of MTR. *NMR Biomed.* **31**(7), e3934. <https://doi.org/10.1002/nbm.3934> (2018).
32. Zhang, X. Y. *et al.* Accuracy in the quantification of chemical exchange saturation transfer (CEST) and relayed nuclear Overhauser enhancement (rNOE) saturation transfer effects. *NMR Biomed.* <https://doi.org/10.1002/nbm.3716> (2017).
33. Heo, H. Y. *et al.* Insight into the quantitative metrics of chemical exchange saturation transfer (CEST) imaging. *Magn. Reson. Med.* **77**(5), 1853–1865. <https://doi.org/10.1002/mrm.26264> (2017).
34. Zhou, J., Heo, H. Y., Knutsson, L., van Zijl, P. C. M. & Jiang, S. APT-weighted MRI: Techniques, current neuro applications, and challenging issues. *J. Magn. Reson. Imaging* **50**(2), 347–364. <https://doi.org/10.1002/jmri.26645> (2019).
35. Suh, C. H. *et al.* Amide proton transfer-weighted MRI in distinguishing high- and low-grade gliomas: A systematic review and meta-analysis. *Neuroradiology* **61**(5), 525–534. <https://doi.org/10.1007/s00234-018-02152-2> (2019).
36. Lee, J., Kim, S. H. & Kang, B. J. Prognostic factors of disease recurrence in breast cancer using quantitative and qualitative magnetic resonance imaging (MRI) parameters. *Sci. Rep.* **10**(1), 7598. <https://doi.org/10.1038/s41598-020-64564-6> (2020).
37. Hainc, N., Stippich, C., Stieltjes, B., Leu, S. & Bink, A. Experimental texture analysis in glioblastoma: A methodological study. *Invest. Radiol.* **52**(6), 367–373. <https://doi.org/10.1097/RLL.0000000000000354> (2017).

Author contributions

E.S., T.S., M.M., S.S.S. wrote the manuscript. E.S., T.S., M.W., S.S.S., L.V.S., C.A.B., C.R., M.M. designed the study. M.W., L.V.S., S.S.S. provided patient data and images. E.S., T.S., M.M. performed data analysis. E.S., T.S. performed region-of-interest delineation. C.A.B., C.R. proofread the manuscript.

Funding

Open Access funding enabled and organized by Projekt DEAL.

Competing interests

MW is a part time employee of Philips Healthcare Switzerland. The remaining authors declare that the research was conducted in the absence of any commercial or financial relationships that could be construed as a potential conflict of interest.

Additional information

Supplementary Information The online version contains supplementary material available at <https://doi.org/10.1038/s41598-021-85168-8>.

Correspondence and requests for materials should be addressed to M.M.

Reprints and permissions information is available at www.nature.com/reprints.

Publisher's note Springer Nature remains neutral with regard to jurisdictional claims in published maps and institutional affiliations.



Open Access This article is licensed under a Creative Commons Attribution 4.0 International License, which permits use, sharing, adaptation, distribution and reproduction in any medium or format, as long as you give appropriate credit to the original author(s) and the source, provide a link to the Creative Commons licence, and indicate if changes were made. The images or other third party material in this article are included in the article's Creative Commons licence, unless indicated otherwise in a credit line to the material. If material is not included in the article's Creative Commons licence and your intended use is not permitted by statutory regulation or exceeds the permitted use, you will need to obtain permission directly from the copyright holder. To view a copy of this licence, visit <http://creativecommons.org/licenses/by/4.0/>.

© The Author(s) 2021